Journal of Molecular Liquids 398 (2024) 124140

Contents lists available at ScienceDirect

Journal of Molecular Liquids

journal homepage: www.elsevier.com/locate/molliq

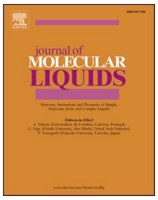

Dicationic ionic liquid crystals: Synthesis, characterization, optical properties, and ionic conductivity of bis(4-oligoethyleneoxyphenyl) viologen bistosylate salts

Pradip K. Bhowmik [a,*], Si L. Chen [a], David King [a], Haesook Han [a], Zane Bolyard [b], Christopher Schmiedl [b], Michael R. Fisch [b], Sanjeev R. Gopal [c], Thamil Selvi Velayutham [c], Alfonso Martinez-Felipe [d]

[a] *Department of Chemistry and Biochemistry, University of Nevada Las Vegas, 4505 S. Maryland Parkway, Box 454003, Las Vegas, NV 89154, USA*
[b] *College of Aeronautics and Engineering, Kent State University, Kent, OH 44242, USA*
[c] *Low Dimensional Materials Research Center, Department of Physics, Faculty of Science, Universiti Malaya, 50603 Kuala Lumpur, Malaysia*
[d] *Chemical Processes and Materials Research Group, School of Engineering, Just Transitions Lab, Centre for Energy Transition, University of Aberdeen, King's College, Old Aberdeen, AB24 3UE, UK*

ARTICLE INFO

Keywords:
Ionic liquid crystals
Differential scanning calorimetry
Polarized optical microscopy
Variable temperature X-ray diffraction
Ionic conductivity
Dielectric spectroscopy

ABSTRACT

Three bis(4-oligoethyleneoxyphenyl) viologen bistosylate salts of different lengths were prepared *via* the Zincke reaction followed by a metathesis reaction with silver tosylate, and their chemical structures confirmed by ^{1}H, ^{13}C nuclear magnetic resonance (NMR), Fourier transform infrared (FTIR) techniques, and elemental analysis. Thermogravimetric analysis (TGA) showed these salts had excellent thermal stabilities, losing just 5 % of their initial mass between 283 and 288 °C. Liquid crystalline phases and transition temperatures were determined by differential scanning calorimetry (DSC), polarizing optical microscopy (POM), and variable temperature X-ray diffraction (VTXRD) techniques. The salts exhibited weak fluorescent emission in dichloromethane and no emission in acetonitrile but exhibited light emission in the solid state. Their absolute quantum yields ranged between 3 and 12 %. Impedance spectroscopy showed that the ionic conductivity of the salts increases with the number of oxyethylene units in the extended viologen moiety. The salt-containing four oxyethylene units at each end reach a conductivity value of 10^{-2} S·cm^{-1}, attributed to its larger molecular flexibility and improved ionic liquid mobility.

1. Introduction

Ionic liquid crystals (ILCs) combine the properties of ionic liquids and liquid crystals (LCs), exhibiting important technological properties and have potential in a wide range of applications [1–8]. For example, the smectic phases of ILCs exhibit significantly enhanced electrical conductivity compared to isotropic ionic liquids, by facilitating 2D pathways for ionic mobility [9–15]. Additionally, organic soft materials offer design flexibility and versatility and have been postulated as components in batteries, capacitors, fuel cells, sensors, and actuators [16–20]. Furthermore, most of these materials, including ILCs, have the potential to be recycled [21–23], making them part of a sustainable future.

The properties of ILCs depend on their cationic and anionic constituents and can be tailored by an appropriate combination of organic cations (e.g., quaternary ammonium, quaternary phosphonium, pyrrolidinium, piperidinium, guanidinium, imidazolium, pyridinium, pyrazolium, and triazolium,) and organic/inorganic anions (e.g., ^{-}Br, $^{-}NO_3$, $^{-}BF_4$, $^{-}CF_3SO_3$, $^{-}PF_6$, $^{-}ClO_4$, ^{-}OTs, $^{-}N(SO_2CF_3)_2$ and ReO_4^{-}). Whilst the above list only includes the monocations and monoanions moieties commonly employed in ILCs [1–8], the synthesis of dicationic, tricationic, and multicationic materials broadens the molecular structural combinations and material versatility of ILCs [24–36]. Recently prepared dicationic viologens have exhibited a variety of smectic phases (SmA, SmC, SmT, and other unidentified Smectic phases) over a broad range of temperatures, from sub-ambient to around 200 °C [37–41].

In addition to improving their thermal stability, the presence of multiple ions can also enhance the lateral interactions involved in

---

* Corresponding author.
E-mail address: pradip.bhowmik@unlv.edu (P.K. Bhowmik).

https://doi.org/10.1016/j.molliq.2024.124140
Received 31 July 2023; Received in revised form 23 January 2024; Accepted 25 January 2024

forming liquid crystal phases and the electrical conductivity of ILCs [37–41]. However, excessive ionic interactions can also lead to high melting points, and increased molecular stiffness that ultimately precludes mesomorphism. Extending the viologen moiety with phenyl residues in multicationic salts has been a good strategy to promote anisotropy through increasing the molecular length-to-width ratio, see for example **(I-VI)** in Fig. 1 [42–45]. To reduce the melting points and obtain ILCs, this must be accompanied by a rational design of the length and composition of the flexible terminations attached to the phenyl cores. More specifically, the design of symmetric or asymmetric ILCs and the polarity of the individual molecular components are paramount to the formation of smectic phases.

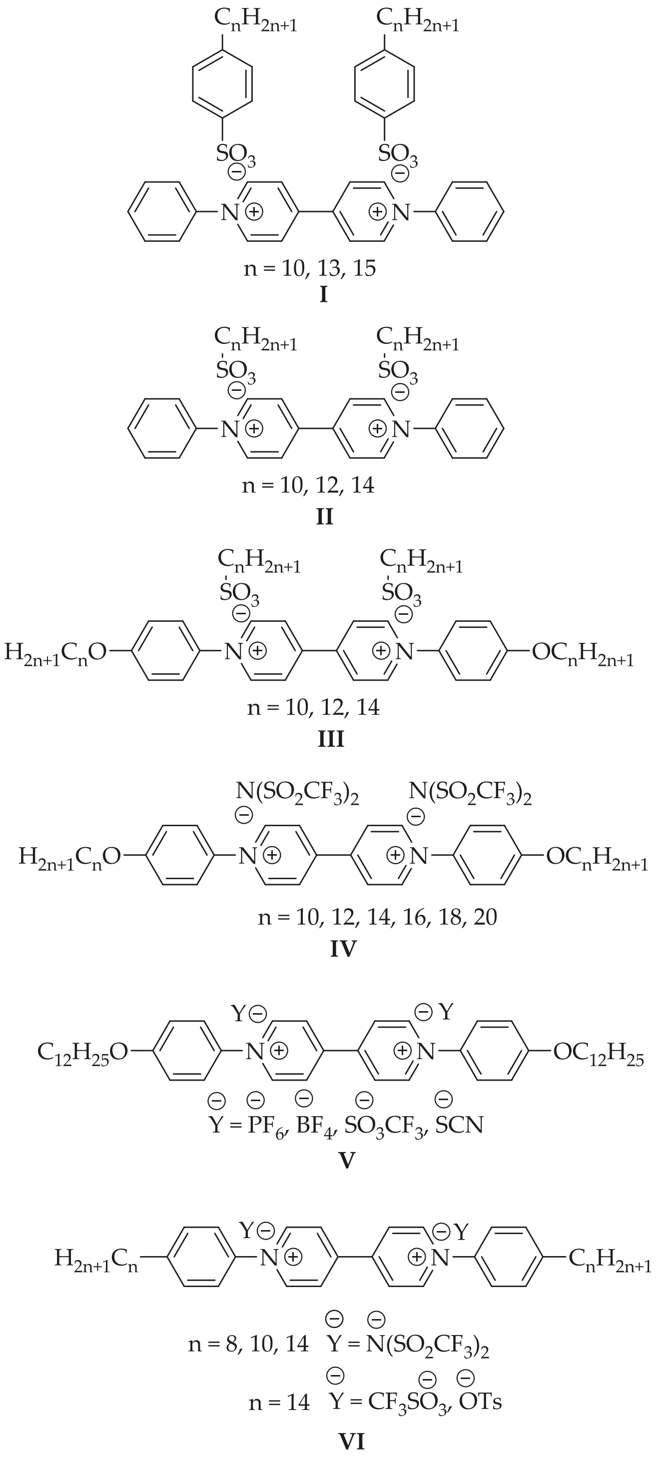

Fig. 1. Chemical structures of extended viologen salts (I-VI) that exhibit SmA phases [42–45].

In a recent work, we assessed a series of extended viologen salts containing oxyethylene groups and bistriflimide ions [46]. Despite obtaining promising results in terms of high electrical conductivity, these materials did not exhibit liquid crystallinity. We speculate that this arose from the presence of strong interactions by a combination of the oxyethylene links and the bistriflimide ions. Whilst these must be beneficial for ionic conductivity, the interactions may restrict the mobility of the terminal chains and ultimately inhibit the formation of mesophases. In this work, we use tosylate as an alternative counterion to bistriflimide to develop new ILCs with future applications as electrolytes. We hypothesize that the higher compatibility of tosylate ions with the extended phenyl core may help promote smectic phases in these new materials and found this to be true.

2. Materials and methods

2.1. General Information

Three phenyl-extended viologen salts, **1** to **3**, containing lateral chains of oxyethylene groups $(CH_2\text{-}CH_2\text{-}O)_n$ of different lengths, n = 1, 2, and 3, and bistosylate counterions were prepared. The general structures and designations for the compounds and their synthetic routes are shown in Scheme 1. All chemicals and solvents used were

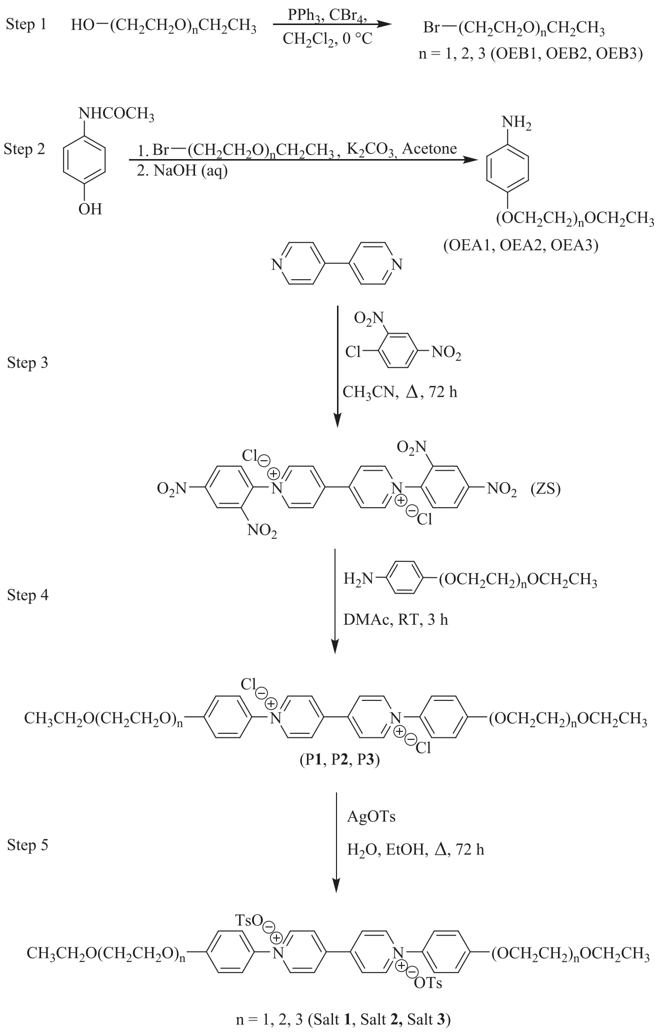

Scheme 1. Multiple steps for the synthesis of ionic liquid crystals **1**–**3**. Note that n = 1 corresponds to one additional oxyethylene.

reagent grade, purchased from commercial suppliers (Acros Organics, Alfa-Aesar, Sigma-Aldrich, and TCI America), and were used as received. The chemical structures of the salts were assessed from the analyses of ^{1}H and ^{13}C nuclear magnetic resonance (NMR) using deuterated methanol (CD_3OD), Fourier transform infrared (FTIR) spectra and elemental analysis. The ^{1}H- NMR and ^{13}C -NMR spectra were recorded by using a VNMR 400 spectrometer operating at 400 and 100 MHz, respectively, at room temperature, and chemical shifts were referenced to tetramethylsilane (TMS). The FTIR spectra of thin films, cast from chloroform solutions of the salts onto NaCl and vacuum dried at 70 °C, were recorded with a Shimadzu infrared spectrometer in transmission mode. Elemental analyses were performed by Atlantic Microlab Inc., Norcross, GA.

2.2. *Synthesis*

The synthesis of **1**–**3** was performed according to Scheme 1 and followed literature procedures [45,47–51]. The detailed procedures and spectroscopic analysis (Figs. S1-S9) are given as Supplementary Information (SI). Data for **1:** Anal. Calc for $C_{44}H_{48}N_2O_{10}S_2$ (828.99): C, 63.75; H, 5.84; N, 3.38; S, 7.74 %. Found C, 63.47; H, 5.67; N, 3.55; S, 7.60 %. Data for **2:** Anal. Calc for $C_{48}H_{56}N_2O_{12}S_2$ (917.09): C, 62.86; H, 6.15; N, 3.05; S, 6.99 %. Found C, 62.81; H, 6.03; N, 3.15; S, 6.96 %. Data for **3:** Anal. Calc for $C_{52}H_{64}N_2O_{14}S_2$ (1005.20): C, 62.13; H, 6.42; N, 2.79; S, 6.38 %. Found C, 61.70; H, 6.43; N, 2.89; S, 6.06 %.

2.3. *Characterization techniques*

The phase transition temperatures of the salts under a nitrogen atmosphere were determined using a TA DSC Q200 module at heating and cooling rates of ± 10 °C·min^{-1}. The differential scanning calorimetry (DSC) temperature axis was calibrated with high-purity indium and tin reference standards. The thermal stability of the salts in nitrogen was assessed by thermogravimetric analysis (TGA) using a TGA Q50 thermobalance at a heating rate of 10 °C·min^{-1}. Polarized optical microscopy (POM) studies were carried out by sandwiching the salts between standard glass coverslips and using a Mettler hot-stage (FP82HT) and controller (FP90) for temperature control. Their phase transitions were observed between cross polarizers using an Olympus BX51 microscope.

Variable-temperature X-ray diffraction (VTXRD) was measured using a Rigaku Screen Machine. The salts in epoxy sealed 1 mm quartz capillaries, were placed inside a Linkam HFS350X-Cap capillary hot stage 62 mm away from the 2D detector, with temperature controlled to an accuracy of ± 0.1 °C. A magnetic field of ∼ 2.5 kG was applied to the samples using a pair of samarium cobalt permanent magnets. The scattering patterns were collected using a Mercury 3 CCD detector with a resolution of 1024 × 1024 pixels (size: 73.2 μm × 73.2 μm) and copper K_α radiation ($\lambda = 1.542$ Å) generated by a microfocus sealed X-ray tube. The data were analyzed using publicly available Fit-2D software to correct for background scattering and generate intensity vs scattering vector, I-q curves.

The room temperature UV–Vis absorption spectra of dichloromethane (DCM) and acetonitrile solutions of the salts **1**–**3** were recorded using a PerkinElmer Fluorescence Spectrometer FL 6500, and the integrating sphere protocol. Absolute quantum yields (AQYs%) of the as-synthesized solid salts were measured with a Horiba Fluorolog fluorimeter (HORIBA Instruments Inc.) also equipped with an integrating sphere. AQY% was calculated as the ratio of light collected in the integrating sphere by the salt to light collected in the same geometry from the standard times 100 %.

Dielectric and conductivity analyses of the salts were performed in a lab-constructed dielectric cell that used two stainless steel electrodes separated by a spacer. The top and bottom electrodes had diameters of 10 mm and 20 mm, respectively. To maintain a separation of 120 μm between the electrodes, we used a spacer made from a fused silica fiber with a diameter of 120 μm. The samples' temperature was controlled using a Lakeshore temperature controller. Dielectric measurements were performed over a frequency range of 40–10^6 Hz using isothermal temperature steps and an impedance analyzer (Agilent 4294). The capacitance C_p and the dielectric loss, D were measured at varying temperatures ranging from 30 to 190 °C depending on the isotropic transition temperature, T_i of the salt. The results were analyzed in terms of complex permittivity, $\varepsilon^* = \varepsilon' - j\varepsilon''$ where ε' is the real dielectric permittivity and ε'' is the imaginary dielectric permittivity and j is the imaginary unit, $j = \sqrt{-1}$. The dielectric permittivity was transformed to the complex conductivity using $\sigma^* = j\omega\varepsilon_0\varepsilon^*$, where ε_0 is the permittivity of vacuum, (8.85*10^{-12}F/m). Before each measurement, the samples were allowed to stabilize at the specified temperature for approximately two minutes, and data was taken on both heating and cooling. Values of direct current conductivity, σ_{DC}, were estimated by extrapolating to low frequencies the plateaus of the real component of the complex conductivity, σ', when plotted against the frequency on double logarithmic graphs.

3. Thermal and ILC properties

3.1. *Thermal stability: TGA*

The thermal stability of salts **1**–**3** was assessed by TGA and the characteristic temperature, T_d is defined as the temperature (℃) at which a 5 % weight loss occurred at a heating rate of 10 °C·min^{-1} with the salt in nitrogen. Despite the presence of flexible oxyethylene groups, the TGA thermograms display relatively high thermal stabilities, exhibiting decomposition temperatures in the range of 283–288 °C (see Fig. 2 and Table 1). This temperature gradually decreased as the number of oxyethylene groups in the terminal chains increased. As expected, the bistosylate salts show lower thermal stabilities than those of the homologous series containing bistriflimide as counterions (311–334 °C) due to the absence of fluorine atoms, and the reactivity of the p-tolyl group [46].

3.2. *ILC phase behavior: DSC, POM, and VTXRD studies*

Thermal properties obtained from DSC measurements and decomposition temperatures obtained from TGA measurements are compiled in Table 1. Fig. 3a shows the DSC thermograms of salt **1**, obtained from its heating and cooling scans (±10 °C·min^{-1}), and Fig. S10 shows its DSC thermograms obtained from its heating and cooling scans (±1 °C·min^{-1}). The first heating cycle exhibits several endotherms associated with its thermal history before melting at 204 °C, and the second heating cycle only shows a broad endotherm at 197 °C. The cooling cycles show the presence of broad exotherms accompanied by shoulder peaks at 170 and 155 °C, indicating crystallization occurring from the melt. Whilst DSC does not determine the phase, VTXRD studies further confirm the crystal-to-isotropic liquid transition at T_m ~~T_i~~ ≈ 208 °C, based on the diffractogram patterns. The endotherms below T_m are associated with several crystal-to-crystal transitions, which reflect polymorphism. Fig. 3b depicts the d-spacings of salt **1** as a function of temperature measured in the second cooling cycle. Several points need to be made. Whilst DSC scan rates of 10 °C min^{-1} are commonly used in LC research [52] and this allows more transitions to be observed, the phase transition temperatures must be verified by other techniques, such as VTXRD or POM. Also note that, at a rate of 1 °C min^{-1} (Supplementary Information), some of the transitions are too small to be observed. As discussed by Neubert [52], samples commonly require several heating and cooling cycles to exhibit reproducible phase behavior. Generally, the second or even subsequent cooling curve is used for determining transition temperatures in POM and VTXRD. Careful phase identification and phase transition temperatures are obtained at cooling rates of 1–2 °C·min^{-1} or even slower. The 1 °C min^{-1} DSC scans indicate the melting temperature, T_m, is 204–205 °C for salt **1**,

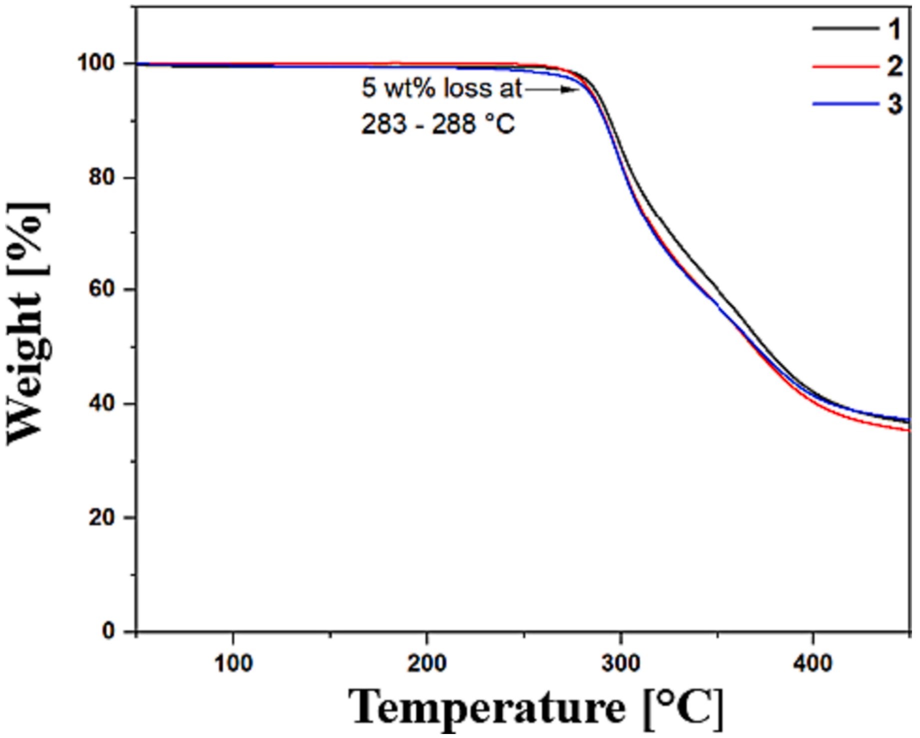

Fig. 2. TGA thermograms of salts **1**, **2**, and **3** obtained at a heating rate of 10 °C·min^{-1} in nitrogen.

Table 1
Transition temperature T(℃) and enthalpies ΔH (kJ/mol, in italics) of the transitions for the salts **1**–**3** obtained from DSC at 10 °C min^{-1} scanning rate, and phase determination from POM and VTXRD.

Salt	Heating/cooling H/C	Crystal	T_m (℃) *ΔH* *(kJ/mol)*	Sm A	T_i (℃) *ΔH* *(kJ/mol)*	Isotropic	LC range (℃)	T_d (℃)
1								288
	1H	*	204 *(25.3)*	–	–	*	–	
	2H	*	197 *(26.7)*	–	–	*	–	
	1C	*	170 *(26.1)*	–	–	*	–	
	2C	*	155 *(24.2)*	–	–	*	–	
	POM	*	–	–	–	*	–	
	XRD	*	208	–	–	*	–	
2								286
	1H	*	184 *(92.2)*	*	216 *(2.6)*	*	32	
	2H	*	182 *(79.4)*	–	–	*	–	
	1C	*	170 *(25.5)*	–	–	*	–	
	2C	*	154 *(22.8)*	–	–	*	–	
	POM	*	–	*	–	–	–	
	XRD	*	182	*	204	*	22	
3								283
	1H	*	153 (37.7)	–	–	–	–	
	2H	*	147	–	–	–	–	
	1C	*	110 *(11.8)*	–	–	–	–	
	2C	*	105 *(12.9)*	–	–	–	–	
	POM	–	–	*	–	–	–	
	XRD	*	170	*	212	*	30 (170–200)	

T_d is the decomposition temperature determined by TGA, Cry means crystal, SmA smectic A and Iso, Isotropic phase. The star indicates the transition was observed, while a hyphen indicates it was not observed.
* There is a two-phase coexistence of the SmA and Isotropic phases from 200 to 212 °C.

183 °C for salt **2** and 153 °C for salt **3**.

Fig. 4a shows the DSC thermograms of salt **2** obtained at heating and cooling rates of ± 10 °C·min^{-1} and Fig. S11 shows its DSC thermograms obtained from its heating and cooling scans (±1 °C·min^{-1}). The first heating cycle is dominated by a large endotherm with a shoulder visible at 184 °C (ΔH_m = 92.2 kJ·mol^{-1}), and a small endotherm visible at 216 °C (2.6 kJ·mol^{-1}), that is absent in the second heating scan. The first cooling cycle exhibits only a single exotherm visible at 170 °C, whilst, in the subsequent heating cycle (2H), an exotherm appears at 117 °C, followed by an endotherm at 182 °C. In the subsequent cooling cycle, there was only an exotherm at 154 °C. In conjunction with POM studies, it was determined that the large endotherm corresponded to the crystal-to-LC phase transition (Fig. 4b) and the small endotherm corresponded to the LC-to-isotropic liquid transition, T_i = 216 °C (in the first heating cycle). In cooling cycles, the exotherms correspond to the LC-to-crystal transitions.

However, no exotherm associated with a liquid-to-LC transition was detected in the thermogram. Based on this DSC first heating scan, **2**

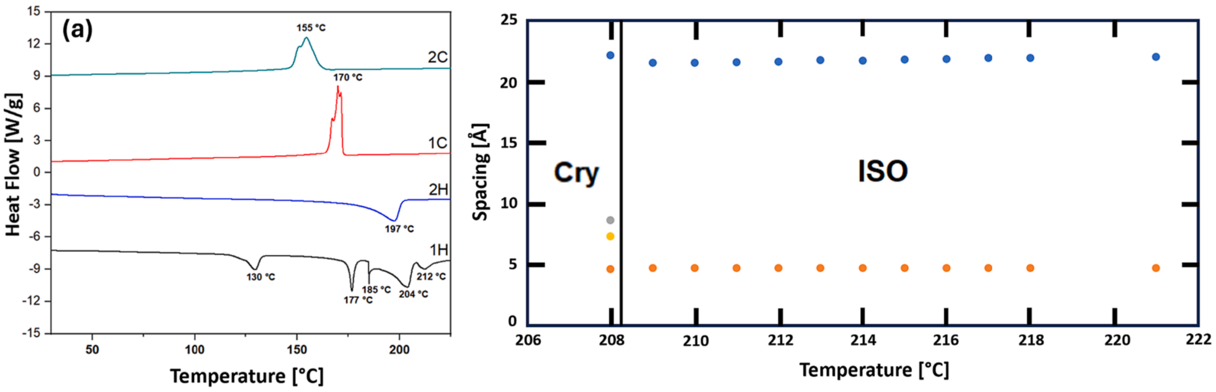

Fig. 3. (a) DSC thermograms of salt **1** obtained at heating and cooling rates of ± 10 °C·min^{-1} in nitrogen (Exo up), (b) The d-spacings of **1** plotted as a function of temperature around the DSC crystal to isotropic transition (T_m = 204 °C) measured in the second cooling cycle. The corresponding VTXRD $T_m \approx 208$ °C.

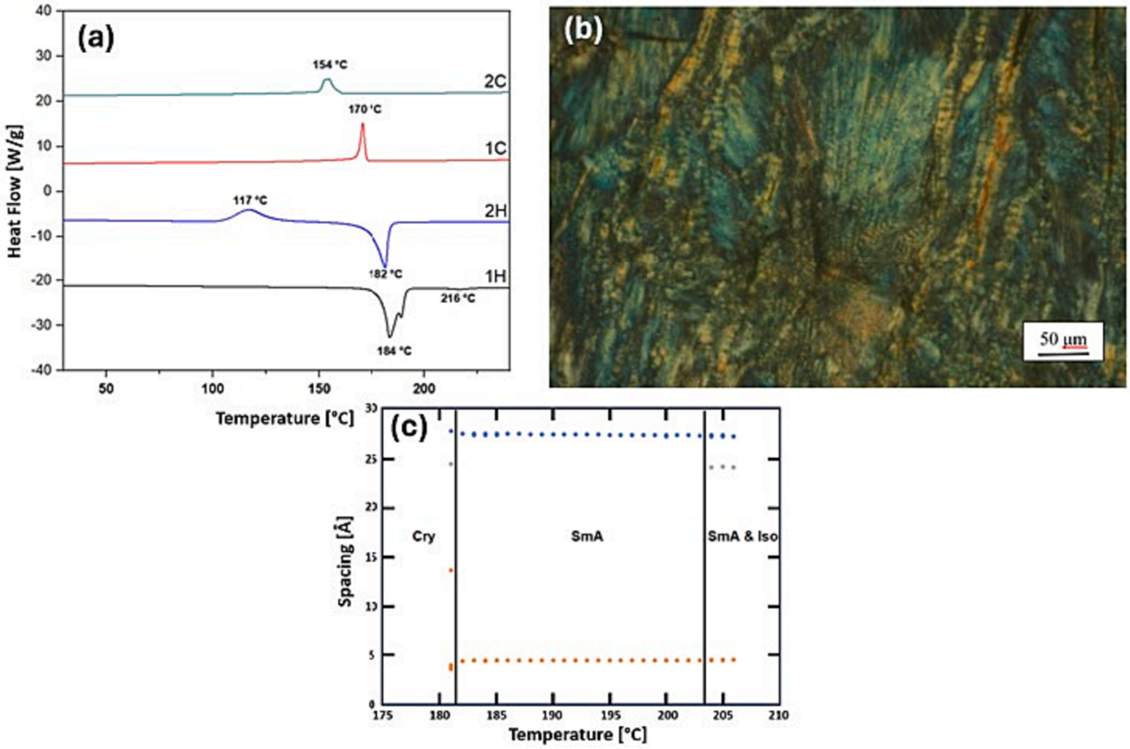

Fig. 4. (a) DSC thermograms of **2** obtained at both heating and cooling rates of 10 °C·min^{-1} in nitrogen (Exo up); (b) photomicrograph of **2** taken by POM (first heating) at 212 °C after melting at 184 °C revealing LC texture; (c) the d-spacings of **2** plotted as a function of temperatures measured on the second cooling cycle. Note the higher sensitivity to phase transitions of VTXRD compared to DSC.

displayed mesomorphism over a 32 °C range. This is larger than the roughly 22 °C range observed using VTXRD measurements. This difference range is most likely related to the different experimental conditions (first heating vs. second cooling) used for these two techniques, heating rates, and the like. Nonetheless, these results are consistent with the corresponding equilibrium VTXRD measurements, which allowed us to identify the liquid crystal phase as a smectic A phase, SmA, see Fig. 4c and Table 1. Both measurements have very similar T_m suggesting temperature rate effects. Its diffractograms contained one inner sharp ring and one outer diffuse ring above the crystal-to-LC transition and an isotropic liquid pattern above the LC-to-liquid transition [53–57]. Its d-spacings in the crystalline, SmA, and isotropic liquid phases were plotted as a function of temperatures and are displayed in Fig. 4c. It is worth mentioning that the diffractograms also indicated the existence of biphasic temperature ranges, where smectic and isotropic regions coexist.

Fig. 5a shows the DSC thermograms of salt **3** obtained at heating and cooling rates of 10 °C·min^{-1} and Fig. S12 shows its DSC thermograms obtained from its heating and cooling scans (±1 °C·min^{-1}). Its thermal properties are comparable with those of **2**, including polymorphism and the formation of a fan-shaped texture typical of SmA phases via POM, Fig. 5b. However, its melting transition (T_m) was located at the highest temperature endotherm with a large enthalpy change (153 °C) in the first heating cycle of the DSC thermogram but not its isotropic liquid transition (T_i). This contrasts with the T_m temperature of 170 °C observed in VTXRD, and once more suggests thermal history effects. In this case, the SmA range determined by VTXRD was wider than **2** (30 vs 22 °C). Phase assignment and stability were further verified with VTXRD studies, which showed similar features as those described above for **2.** The d-spacings for salt **3** in the crystalline, SmA, and liquid phases, are

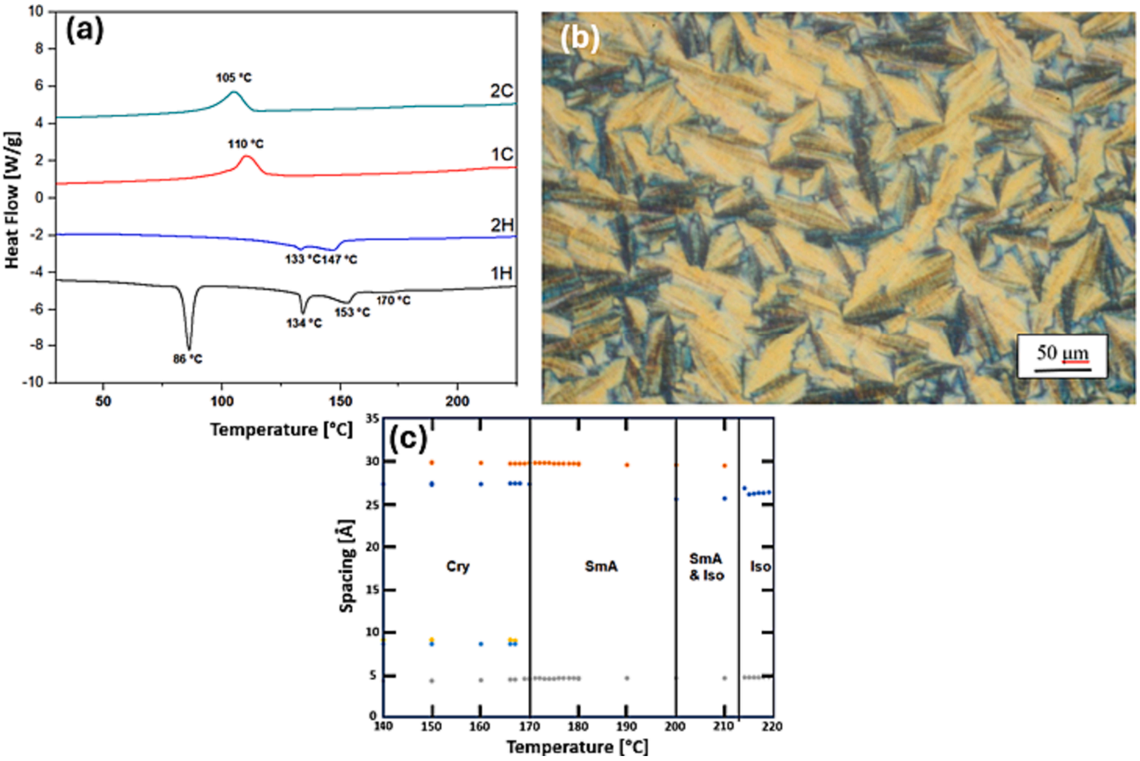

Fig. 5. (a) DSC thermograms of **3** obtained at both heating and cooling rates of 10 °C·min^{-1} in nitrogen (Exo up), (b) Photomicrograph of **3** taken at 200 °C on first heating after its melting transition at 153 °C revealing the fan-shaped texture of SmA, (c) The d-spacings of **3** plotted as a function of temperatures (different colors correspond to different diffracted line) measured in the second cooling cycle. The POM and VTXRD data support the liquid crystalline phase is a smectic and a liquid crystalline range of roughly 30 °C.

displayed in Fig. 5c suggesting its layer spacings increased with increasing chain length.

The DSC and XRD studies indicate that thermal history and possibly heating rate (note the transition at 247 °C on the second heating of salt 1 at 1 °C min^{-1}) can be important in these studies. While the maximum temperature of the 1℃ min^{-1} trace is well below the decomposition temperature of 288 °C, some chemical change may have occurred. XRD samples were routinely taken to temperatures approximately 20 °C above the first isotropic data points shown. As indicated by the associated DSC thermograms, this is due to phase transitions tending to occur at lower temperatures when undergoing cooling when compared to those from heating.

*3.3. Optical spectroscopic properties of salts **1**–**3***

The presence of the extended viologen moieties promotes an optical response in these salts, which was examined by UV–Vis and photoluminescence spectroscopies, both in DCM (dichloromethane) and acetonitrile (ACN), as well, as in the solid state. In DCM, the salts show a broad absorption peak, obtaining λ_{max} at 390, 389, and 389 nm, whilst in ACN they showed a broad absorption signal, with maxima at λ_{max} = 377, 378, and 399 nm, for **1**–**3,** respectively**.** Using the respective Beer-Lambert plots, the calculated molar absorption coefficients are large, ≈20,000 M^{-1}cm^{-1} for all three salts in both solvents. Their light emissions in both DCM and ACN were too weak to be measured or detected.

These results prompted us to measure the light emission at 546, 508, and 533 nm, (Fig. S13) of the salts in the solid state. From these measurements, we determined the absolute quantum yields. Interestingly, their light emissions in the solid state were quite respectable: 7, 12, and 3 %, respectively. Generally, quantum yields are low in the solid state because of aggregation-caused quenching (ACQ), while quantum yields are high in solutions because aggregation phenomena do not occur. These results suggest that the salts undergo aggregation-induced emission (AIE) in the solid state, which has been studied for many organic luminophores for the last two decades and has pinpointed the interest of the viologens as promising materials for potential applications in optoelectronic technologies [58,59].

4. Electrical conductivity and dielectric response

The real component of the complex conductivity, $\sigma^{'}$, for all three materials as a function of frequency, *f*, at a temperature of 30 °C is plotted on a log–log scale in Fig. 6. Conductivity increases with the number of the oxyethylene units located at both ends of the extended viologen moiety, and salt **3**, containing four oxyethylene units, exhibits the highest direct current conductivity at room temperature (30 °C),

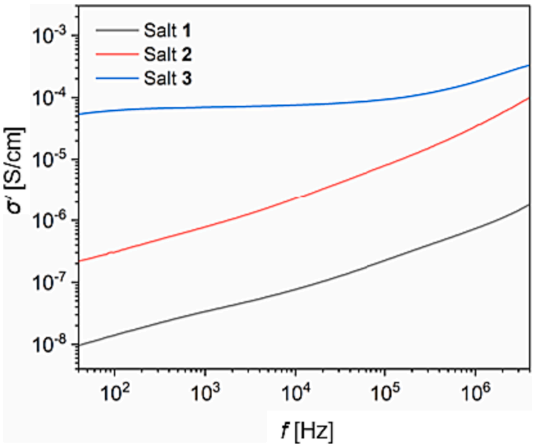

Fig. 6. The real conductivity, $\sigma^{'}$ as a function of frequency for the three salts at 30 °C.

with $\sigma_{DC} \sim 4 \text{ x } 10^{-5}$ S/cm. Longer oxyethylene units in the salts' structure may increase the flexibility of the molecule [60] promoting the movement of ions within the ionic liquid and leading to higher conductivity [61]. This is consistent with the decrease in the melting points reported in Table 1. It is worth mentioning, nevertheless, that longer oxyethylene may also increase the relative concentration of sites available for the solvation of ions [61], and reduce ion-ion interactions [62,63]. However, whilst extending the end chains could be seen as an opportunity to yield higher conductivities, this may also result in strong ionic complexation, and result in mobility hindrance [64]. Our results in Fig. 6 may arise as a combination of both factors.

The high electrical conductivity suggests these materials exhibit an interesting response to applied electric fields. The response of a material to an applied electric field is given by its complex permittivity, ε^*. This quantity has a term that corresponds to the stored energy, which is proportional to ε', and a dissipative term corresponding to the energy loss, which is proportional to ε''. These are out of phase (orthogonal) and combine to form the complex permittivity, $\varepsilon^* = \varepsilon' + j\varepsilon''$, [65]. Due to its high room temperature conductivity, we have investigated the effect of temperature on ε^* of salt **3,** and display results, obtained on heating from 30 to 190 °C, and subsequently cooling back to 30 °C at rates of ± 1 °C·min^{-1} in Fig. 7. While the thermal history is different, the XRD sample was taken to 220 °C with no noticeable change; therefore, we believe that the different temperature range does not have any effect on our conductivity results. The high ε' values, see Fig 7(a), are indicative of a strong dielectric response, associated with the existence of polarizable groups in the molecule. The occurrence of ionic conductivity, Fig. 6, results in an increase of ε'' at low frequencies even at low temperatures, Fig. 7(b), which may foreshadow dielectric relaxations in that frequency range. As expected, the dielectric response increases at higher temperatures. The temperature-frequency relationships will be explained in more detail later. Focusing on the ε' values obtained at 3 kHz on heating, two peaks were observed at 49 °C and 92 °C, followed by a plateau and further drop above 170 °C. This latter value fits well with the melting temperature of this sample reported in Table 1 and suggests that the crystal to smectic transition is either not visible in Fig. 7(c) or takes place at lower temperatures within the cells (T > 92 °C), due to strong alignment effects between electrodes and the ionic liquid that promote smectic organizations [2]. On cooling, the real permittivity remained approximately constant at $\varepsilon' \sim 10^4$, above 160 °C, subsequently it dropped to $\varepsilon' \sim 10^2$ at 158 °C. This drop could indicate sudden crystallization of the salt inside the cell.

The temperature response of the complex electrical conductivity of salt **3** is displayed in Fig. 8, and the temperature-dependent behavior of salt **1** and salt **2** is given in Figs. S14 and S15. The double logarithmic plots of the real component of the conductivity (σ') vs frequency and temperature exhibit three distinct regions, see Fig. 8(a). At lower temperatures and high frequencies, the conductivity is governed by strong dispersion effects where the conductivity is significantly influenced by the frequency of the applied signal. At intermediate frequencies, the ions have enough time to hop between electrodes and the appearance of plateaus in σ' demonstrates the occurrence of DC conductivity. Lastly, at low frequencies, σ' decreases due to electrode polarization effects caused by the accumulation of charges at the electrode surfaces [66,67]. The existence of significant polarization is consistent with the appearance of a maximum in the imaginary part of the conductivity, σ'', shown in Fig. 8 (b).

At higher temperatures, the conductivity of the ionic liquid shows an upward trend, with the σ'' relaxation peak shifting to higher frequencies at higher temperatures. Such an increase in conductivity can be attributed to two possible effects. On the one hand, temperature may activate more ionic sites due to an increase in the molecular mobility of the salt, and larger free volume available for ion hopping. At the same time, ions will have more thermal energy, and hence diffusion will be promoted. These two effects also reflect the shift of the DC conductivity region towards higher frequencies on heating in Fig. 8(a) since the ions require less time to completely relax into their equilibrium positions between successive cycles of the applied electric field.

The thermal activation energy of the conductivity was obtained via Arrhenius plots shown in Fig. 9. The DC conductivity values σ_{DC} were

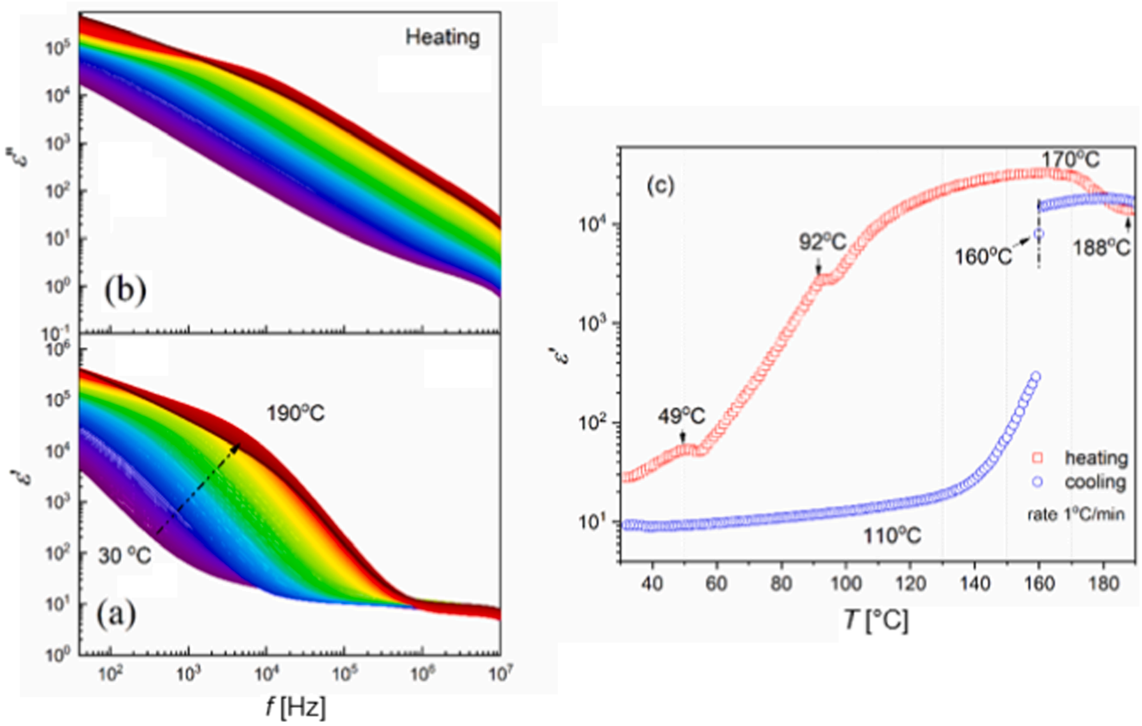

Fig. 7. Isothermal Bode plots of the complex permittivity ($\varepsilon^* = \varepsilon' - j\varepsilon''$) for salt **3**, showing the real (a) and imaginary (b) components. Different colors correspond to different temperatures. (c) Temperature dependence of ε' measured at 3 kHz.

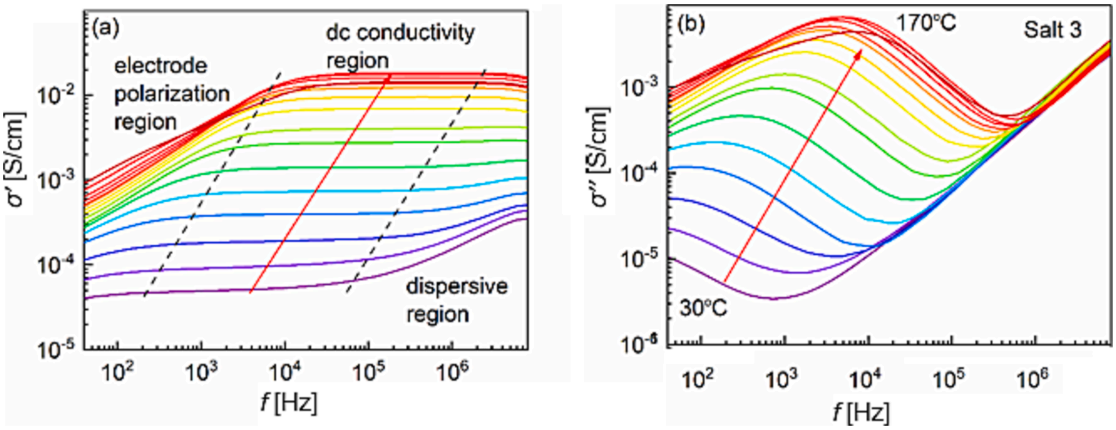

Fig. 8. Temperature variation of the complex conductivity, σ*, for salt **3**: (a) real component, σ'; (b) imaginary component, σ''. Different colors indicate different temperatures.

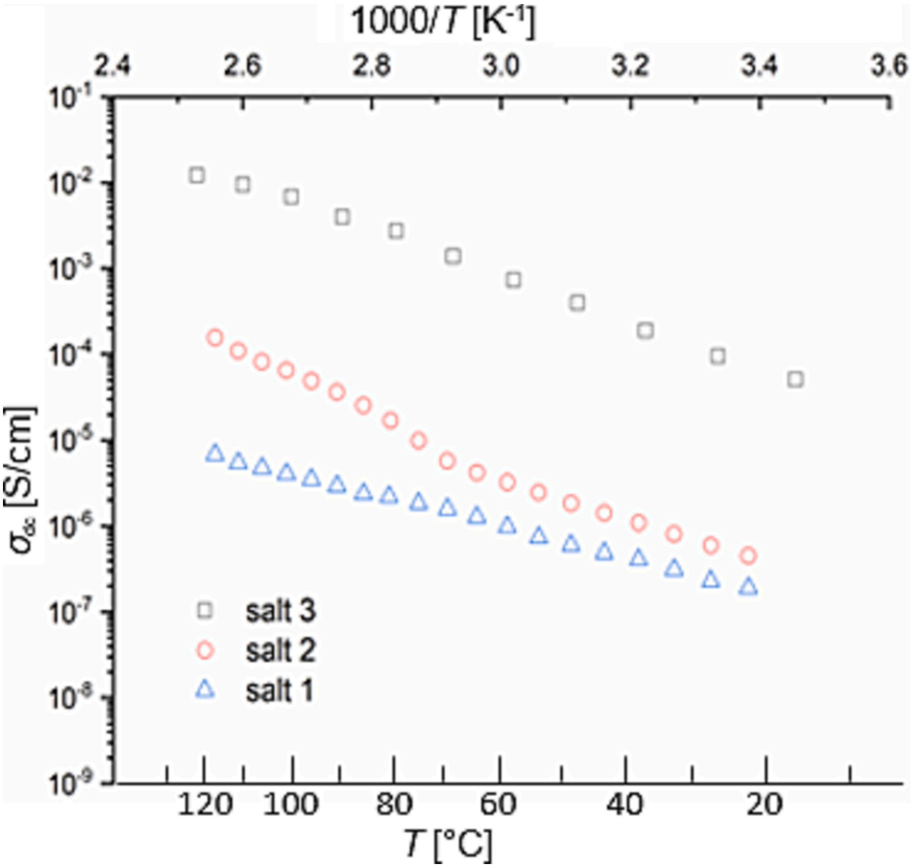

Fig. 9. DC conductivity on a logarithmic scale as a function of 1/T with T measured in Kelvin.

estimated by extrapolating the constant σ' ranges to $f \to 0$ at each temperature. At low temperatures, in the crystalline phase(s), the DC conductivity follows an exponential behavior, and the activation energies E_a is calculated using the Arrhenius equation,

$$\sigma_{dc} = \sigma_o \exp\left(\frac{E_a}{RT}\right)$$

where R is the gas constant, 8.31 J mol^{-1} K^{-1}, T is the absolute temperature, and σ_o is a pre-exponential term. Salts **1** and **2** have activation energies of 39 kJ·mol^{-1} and 49·kJ.mol^{-1} while salt **3** exhibits 57 kJ·mol^{-1}, respectively, which means that the salt with the highest conductivity (four oxyethylene units; salt **3**) also has the highest activation energy. Even though one normally expects a higher conductivity to be associated with lower activation energy [68], it is important to note that activation energy alone does not solely determine conductivity. Other factors, such as the number of charge carriers and their mobility, may significantly influence conductivity.

Indeed, the higher conductivity exhibited for salt **3** (despite its high E_a values) can be explained by the increased flexibility of the longer oxyethylene units. This increased mobility may offset the higher activation energy, resulting in a higher conductivity compared to the other salts. We also speculate that the formation of more well-defined smectic layers promoted by longer oxyethylene chains also increases the conductivity. In Fig. 10(a) we have included the molecular lengths

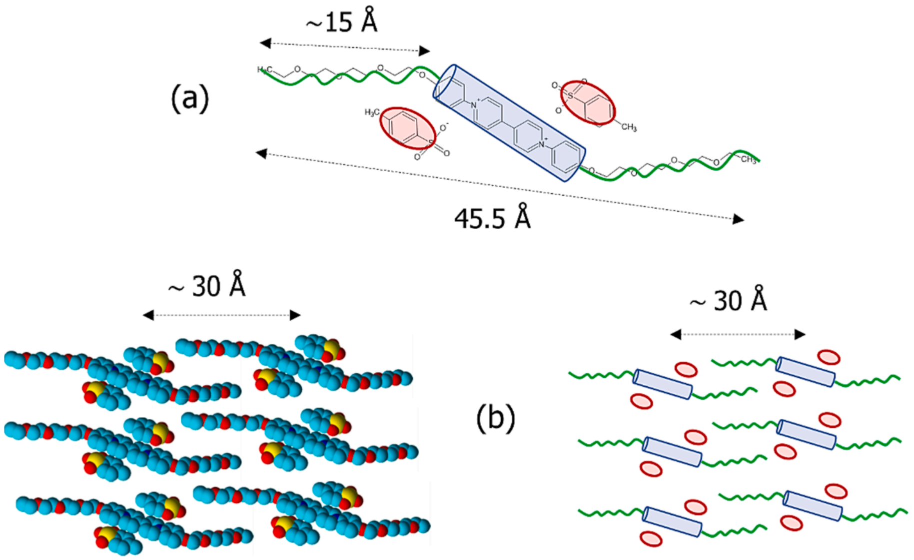

Fig. 10. (a) Molecular model and lengths for salt **3**, estimated with ACD Software; (b) schematical sketches of a potential smectic nanostructure based on the X-ray diffraction results from Fig. 5, indicating aromatic and ethylene oxide regions.

associated with salt **3,** and in Fig. 10(b) we have sketched a representation of the smectic phase, consistent with the distances calculated by VTXRD and shown in Fig. 5. The formation of such nanostructure would allow for sufficient free volume to promote molecular and ionic mobility. These data also suggest that some alignment of the molecules is carried from the LC to the crystalline phase. Determining which mechanism is responsible for the high DC conductivity remains an intriguing question that will be further explored.

5. Conclusions

Three extended viologens containing bistosylate as counterions were successfully synthesized using Zincke reactions, followed by metathesis, and displayed high thermal stabilities (thermal decomposition temperatures above 280 °C). The first member in the series (with the shortest terminal chain containing two repeating oxyethylene units, $n = 1$) was a high melting temperature salt (204 °C), and the second and third members ($n = 2$ and 3) showed SmA phases above their melting points (184 and 153 °C, respectively) in first heating cycles of DSC thermograms. The second member had a liquid crystalline range of 32 degrees, but the third member showed no T_i transition. The range for the second member determined by VTXRD after multiple heating and cooling steps exhibited an LC temperature range approximately 10 degrees smaller than that by DSC. Whilst the salts showed weak (or non-existent) light emission in relatively non-polar solvents (DCM and ACN), they exhibited light emission in the solid state presumably promoted by aggregation-induced emission, with moderate absolute quantum yields between 3 and 12 %. Electrical conductivity increases with the length of the oxyethylene units in the extended viologen moiety, reaching σ_{dc} 10^{-2} S·cm^{-1}, in the crystalline phase near 100 °C close to those values exhibited by commercial electrolytes used in fuel cells or batteries [69,70], and higher than many other liquid crystalline materials [10,71–77]. The presence of longer oxyethylene units enhances the flexibility of the molecules, and it is proposed that this promotes ion movement within the salts and results in higher electrical conductivity. As expected, both dielectric permittivity and conductivity increase with temperature, which can be beneficial to yield controllable electrolytes in their liquid crystalline mesophases. The combination of light emission and conductivity will be investigated to design new ionic liquid crystals that can be used in optical and energy device applications.

CRediT authorship contribution statement

Pradip K. Bhowmik: Writing – review & editing, Writing – original draft, Supervision, Project administration, Investigation, Funding acquisition, Data curation, Conceptualization. **Si L. Chen:** Writing – original draft, Validation, Methodology, Investigation, Formal analysis, Data curation, Conceptualization. **David King:** Writing – original draft, Visualization, Validation, Methodology, Formal analysis, Data curation, Conceptualization. **Haesook Han:** Writing – review & editing, Writing – original draft, Visualization, Validation, Resources, Methodology, Investigation, Formal analysis, Data curation, Conceptualization. **Zane Bolyard:** Writing – original draft, Visualization, Validation, Software, Resources, Methodology, Formal analysis, Data curation. **Christopher Schmiedl:** Writing – original draft, Visualization, Validation, Software, Resources, Methodology, Formal analysis, Data curation, Conceptualization. **Michael R. Fisch:** Writing – review & editing, Writing – original draft, Visualization, Supervision, Project administration, Methodology, Investigation, Funding acquisition, Conceptualization. **Sanjeev R. Gopal:** Writing – original draft, Visualization, Validation, Software, Methodology, Formal analysis, Data curation, Conceptualization. **Thamil Selvi Velayutham:** Writing – review & editing, Writing – original draft, Validation, Supervision, Resources, Project administration, Methodology, Investigation, Funding acquisition, Formal analysis, Data curation, Conceptualization. **Alfonso Martinez-Felipe:** Writing – review & editing, Writing – original draft, Validation, Supervision, Resources, Project administration, Methodology, Investigation, Funding acquisition, Formal analysis, Data curation, Conceptualization.

Declaration of competing interest

The authors declare that they have no known competing financial interests or personal relationships that could have appeared to influence the work reported in this paper.

Data availability

Data will be made available on request.

Acknowledgments

PKB sincerely acknowledges the Knowledge Fund that is administered by the Nevada Governor's Office of Economic Development

(GOED) and the University of Nevada Las Vegas (UNLV). HH sincerely acknowledges the Faculty Opportunity Award (FOA) that is administered by the Office of Sponsored Programs (OSP) at UNLV. MRF sincerely acknowledges the Petroleum Research Fund (Grant 59345-ND7) and National Science Foundation USA (Grant NSF-DMR-2211347) for their support of this research. TSV acknowledges the Ministry of Higher Education of Malaysia through the Fundamental Research Grant Scheme [FRGS/1/2018/STG07/UM/02/6]. AMF would like to thank the Carnegie Trust for the Universities of Scotland, for the Research Incentive Grant RIG008586, the Royal Society and Specac Ltd., for the Research Grant RGS\R1\201397, and the Royal Society of Chemistry for the award of a mobility grant (M19-0000).

Appendix A. Supplementary data

Supplementary data to this article can be found online at https://doi.org/10.1016/j.molliq.2024.124140.

References

[1] A.A. Fernandez, P.H.J. Kouwer, Key developments in ionic liquid crystals, Int. J. Mol. Sci. 17 (2016) 731, https://doi.org/10.3390/ijms17050731.

[2] K. Goossens, K. Lava, C.W. Bielawski, K. Binnemans, Ionic liquid crystals: versatile materials, Chem. Rev. 116 (2016) 4643–4807, https://doi.org/10.1021/cr400334b.

[3] V. Cîrcu, Ionic liquid crystals based on pyridinium salts, in: S. Handy (Ed.), Progress and Developments in Ionic Liquids, London, UK, Intech, 2017, pp. 285–311.

[4] S.J. Devaki, R. Sasi, Ionic liquids/ionic liquid crystals for safe and sustainable energy storage systems, in: S. Handy (Ed.), Progress and Developments in Ionic Liquids, London, UK, Intech, 2017, pp. 316–336.

[5] T. Ichikawa, T. Kato, H. Ohno, Dimension control of ionic liquids, Chem. Commun. 55 (2019) 8205–8214, https://doi.org/10.1039/C9CC04280F.

[6] K. Salikolimi, A.A. Sudhakar, Y. Ishida, Functional ionic liquid crystals, Langmuir 36 (2020) 11702–11731, https://doi.org/10.1021/acs.langmuir.0c01935.

[7] N. Kapernaum, A. Lange, M. Ebert, M.A. Grunwald, C. Haege, S. Marino, A. Zens, A. Taubert, F. Giesselmann, S. Laschat, Current topics in ionic liquid crystals, Chempluschem. 87 (2022) e202100397.

[8] M. Arkas, M. Douloudi, M. Vardavoulias, T. Katsika, Lamellar tetragonal symmetry of amphiphilic thermotropic ionic liquid crystals in the framework of other closely related highly ordered structures, Symmetry 14 (2022) 394, https://doi.org/10.3390/sym14020394.

[9] J.-D. Hwang, P.-Y. Chen, S.-W. Ding, C. Wi Ong, Effect of noncovalent dispersion of poly(ethylene oxide) in columnar polyether-based discotic liquid crystal on the ionic conductivity and dynamics of lithium ions, Crystals 9 (12) (2019) 627, https://doi.org/10.3390/cryst9120627.

[10] T. Kato, M. Yoshio, T. Ichikawa, B. Soberats, H. Ohno, M. Funahashi, Transport of ions and electrons in nanostructured liquid crystals, Nat. Rev. Mater. 2 (4) (2017) 17001, https://doi.org/10.1038/natrevmats.2017.1.

[11] A. Martinez-Felipe, Liquid crystal polymers and ionomers for membrane applications, Liq. Cryst. 38 (11–12) (2011) 1607–1626, https://doi.org/10.1080/02678292.2011.624201.

[12] B.K. Cho, Nanostructured organic electrolytes, RSC Adv. 4 (1) (2014) 395–405, https://doi.org/10.1039/C3RA45044A.

[13] J. Sakoda, M. Yoshio, T. Ichikawa, H. Ohno, T. Kato, 2D assemblies of ionic liquid crystals based on imidazolium moieties: formation of ion-conductive layers, New J. Chem. 39 (6) (2015) 4471–4477, https://doi.org/10.1039/C5NJ00085H.

[14] T. Liang, H.P.C. van Kringen, D.J. Mulder, S. Tan, Y. Wu, Z. Bornean, K. Nijmeijer, A.P.H.J. Schenning, Anisotropic dye adsorption and anhydrous proton conductivity in smectic liquid crystal networks: The role of cross-link density, order, and orientation, ACS Appl. Mater. Interfaces 9 (40) (2017) 35218–35225, https://doi.org/10.1021/acsami.7b09386.

[15] B. Soberats, M. Yoshio, T. Ichikawa, H. Ohno, T. Kato, Zwitterionic liquid crystals as 1D and 3D lithium ion transport media, J. Mater. Chem. A 3 (2015) 11232–11238, https://doi.org/10.1039/C5TA00814J.

[16] R. Sasi, S. Sarojam, S. Devaki, High performing bio-based ionic liquid crystal electrolytes for supercapacitors, ACS Sustainable Chem. Eng. 4 (2016) 3535–3543, https://doi.org/10.1021/acssuschemeng.6b00585.

[17] T. Kato, J. Uchida, T. Ichikawa, T. Sakamoto, Functional liquid crystals towards the next generation of materials, Angew. Chem. Int. Ed. 57 (16) (2018) 4355–4371, https://doi.org/10.1002/anie.201711163.

[18] V. Vallem, Y. Sargolzaeiaval, M. Ozturk, Y.-C. Lai, M.D. Dickey, Energy harvesting and storage with soft and stretchable materials, Adv. Mater. 33 (19) (2021) 2004832, https://doi.org/10.1002/adma.202004832.

[19] J. Uchida, B. Soberats, M. Gupta, T. Kato, Advanced Functional Liquid Crystals 34 (23) (2022) 2109063, https://doi.org/10.1002/adma.202109063.

[20] A. Martinez-Felipe, D. Zaton, M. Castillo-Valles, A. Baldini, J. Pease, N. Leader, N.F. K. Arizin, M. Giacinti-Baschetti, M.B. Ros, Bent-core liquid crystals joining the ethylene-oxide/lithium ion tandem: Ionic conductivity and dielectric response towards new electrolytes for energy applications, J. Mol. Liq. 390 (2023) 123100, https://doi.org/10.1016/j.molliq.2023.123100.

[21] D.T. Do, A.R. Schmitzer, Intramolecular Diels Alder reactions in highly organized imidazolium salt-based ionic liquid crystals, RSC Adv. 5 (2015) 635–639, https://doi.org/10.1039/C4RA11693C.

[22] D.T. Do, A.R. Schmitzer, Highly ordered rectangular columnar ionic liquid crystals: Medium for intramolecular Diels Alder reactions, ChemistrySelect 1 (2016) 2448–2453, https://doi.org/10.1002/slct.201600713.

[23] D.W. Bruce, Y. Gao, J.N. Canongia Lopez, K. Shimizu, J.M. Slattery, Liquid-crystalline ionic liquids as ordered reaction media for the Diels-Alder reaction, Chem. Eur. J. 22 (2016) 16113–16123, https://doi.org/10.1002/chem.201602965.

[24] M. Trill, R. Pleixats, T. Parella, C. Blanc, P. Dieudonné, Y. Guari, M.W.C. Man, Ionic liquid crystals based on mesitylene-containing bis- and trisimidazolium salts, Langmuir 24 (2008) 259–265, https://doi.org/10.1021/la702305t.

[25] K. Tanabe, Y. Suzui, M. Hasegawa, T. Kato, Full-color tunable photoluminescent ionic liquid crystals based on tripodal pyridinium, pyridinium, and quinolinium salts, J. Am. Chem. Soc. 134 (2012) 5652–5661, https://doi.org/10.1021/ja3001979.

[26] S. Asaftei, M. Ciobanu, A.M. Lepadatu, E. Song, U. Beginn, Thermotropic ionic liquid crystals by molecular assembly and ion pairing of 4,4′-bipyridinium derivatives and tris(dodecyl oxy)benzenesulfonates in a non-polar solvent, J. Mater. Chem. 22 (2012) 14426–14437, https://doi.org/10.1039/C2JM31830J.

[27] L.A. Robertson, M.R. Schenkel, B.R. Wiesenauer, D.L. Gin, Alkyl-bis(imidazolium) salts: a new amphiphile platform that forms thermotropic and non-aqueous lyotropic bicontinuous cubic phases, Chem. Commun. 49 (2013) 9407–9409, https://doi.org/10.1039/C3CC44452J.

[28] M.R. Schenkel, R. Shao, L.A. Robertson, B.R. Wiesenauer, N.A. Clark, D.L. Gin, New ionic organic compounds containing a linear tris(imidazolium) core and their thermotropic liquid crystal behavior, Liq. Cryst. 40 (2013) 1067–1081, https://doi.org/10.1080/02678292.2013.798692.

[29] M.R. Schenkel, J.B. Hooper, M.J. Moran, L.A. Robertson, D. Bedrov, D.L. Gin, Effect of counter-ion on the thermotropic liquid crystal behaviour of bis(alkyl)-tris (imidazolium salt) compounds, Liq. Cryst. 41 (2014) 1668–1685, https://doi.org/10.1080/02678292.2014.948087.

[30] M. Yang, K. Stappert, A.-V. Mudring, Bis-cationic ionic liquid crystals, J. Mater. Chem. C 2 (2014) 458–473, https://doi.org/10.1039/C3TC31368A.

[31] F. D'Anna, R. Noto, Di- and tricationic organic salts: An overview of their properties and applications, Eur. J. Org. Chem. (2014) 4201–4223. http://portale.unipa.it/dipartimenti/stebicef.

[32] G. Casella, V. Causin, F. Rastrelli, G. Saielli, Viologen-based ionic liquid crystals: induction of a smectic A phase by dimerization, Phys. Chem. Chem. Phys. 16 (2014) 5048–5051, https://doi.org/10.1039/C3CP54628D.

[33] G. Casella, V. Causin, F. Rastrelli, G. Saielli, Ionic liquid crystals based on viologen dimers: tuning the mesophormism by varying the conformational freedom of the ionic layer, Liq. Cryst. 43 (2016) 1161–1173, https://doi.org/10.1080/02678292.2016.1161852.

[34] P.K. Bhowmik, A. Chang, J. Kim, E.J. Dizon, R.C.G. Principe, H. Han, Thermotropic liquid- crystalline properties of viologen containing 4-n-alkylbenzenesulfonates, crystals 9 (2019) 77. https://doi.org/10.3390/cryst9020077.

[35] H. Chae, Y.-H. Lee, M. Yang, W.-J. Yoon, D.K. Yoon, K.-U. Jeong, Y.H. Song, U. H. Choi, M. Lee, Interesting phase behaviors and ion-conducting properties of dicationic N- alkylimidazolium tetrafluoroborate salts, RSC Adv. 9 (2019) 3972–3978, https://doi.org/10.1039/C8RA09208G.

[36] Y. Song, X. Tang, S. Kong, L. Bai, X. He, F. Meng, Synthesis and characterization of hexamethylenetetramine-based ionic liquid crystals, J. Mol. Struc. 1178 (2019) 135–141, https://doi.org/10.1016/j.molstruc.2018.09.090.

[37] P.K. Bhowmik, H. Han, J.J. Cebe, R.A. Burchett, A. Acharya, S. Kumar, Ambient temperature thermotropic liquid crystalline viologen bis(triflimide) salts, Liq. Cryst. 30 (2003) 1433–1440, https://doi.org/10.1080/02678290310001621895.

[38] P.K. Bhowmik, H. Han, I.K. Nedeltchev, J.J. Cebe, Room-temperature thermotropic ionic liquid crystals: viologen bis(triflimide) salts, Mol. Cryst. Liq. Cryst. 419 (2004) 27–46, https://doi.org/10.1080=15421400490478272.

[39] P.K. Bhowmik, S.T. Killarney, J.R.A. Li, J.J. Koh, H. Han, L. Sharpnack, D.M. Agra-Kooijman, M.R. Fisch, S. Kumar, Thermotropic liquid-crystalline properties of extended viologen bis(triflimide) salts, Liq. Cryst. 45 (2018) 872–885, https://doi.org/10.1080/02678292.2017.1397213.

[40] V. Causin, G. Saielli, Effect of asymmetric substitution on the mesomorphic behaviour of low-melting viologen salts of bis(trifluoromethanesulfonyl)amide, J. Mater. Chem. 19 (2009) 9153–9162, https://doi.org/10.1039/B915559G.

[41] P.K. Bhowmik, O. Noori, S.L. Chen, H. Han, M.R. Fisch, C.M. Robb, A. Variyam, A. Martinez-Felipe, Ionic liquid crystals: synthesis and characterization via NMR, DSC, POM, X-ray diffraction and ionic conductivity of asymmetric viologen bistriflimide salts, J. Mol. Liq. 328 (2021) 115370, https://doi.org/10.1016/j.molliq.2021.115370.

[42] Y. Haramoto, M. Yin, Y. Matukawa, S. Ujiie, M. Nanasawa, A new ionic liquid crystal compound with viologen group in the principal structure, Liq. Cryst. 19 (1995) 319–320.

[43] R.-T. Wang, G.-H. Lee, C.K. Lai, Anion-induced ionic liquid crystals of diphenylviologens, J. Mater. Chem. C 6 (2018) 9430–9444, https://doi.org/10.1039/C8TC03090A.

[44] L. Veltri, G. Cavallo, A. Beneduci, P. Metrangolo, G.A. Corrente, M. Ursini, R. Romeo, G. Terraneo, B. Gabriele, Synthesis and thermotropic properties of new green electrochromic ionic liquid crystals, New J. Chem. 43 (2019) 18285–18293. https://pubs.rsc.org/en/content/articlepdf/2019/nj/c9nj03303c.

[45] P.K. Bhowmik, M.K.M. Al-Karawi, S.T. Killarney, E.J. Dizon, A. Chang, J. Kim, S. L. Chen, R.C.G. Principe, A. Ho, H. Han, H.D. Mandal, R.G. Cortez, B. Gutierrez, K. Mendez, L. Sharpnack, D.M. Agra-Kooijman, M.R. Fisch, S. Kumar, Thermotropic liquid-crystalline and light-emitting properties of bis(4-alkoxyphenyl) viologen bis(triflimide) salts, Molecules 25 (2020) 2435, https://doi.org/10.3390/molecules25102435.

[46] P.K. Bhowmik, S.L. Chen, H. Han, K.A. Ishak, T.S. Velayutham, U. Bendaoud, A. Martinez-Felipe, Dicationic ionic liquids based on bis(4-oligoethyleneoxyphenyl) viologen bistrfilimde salts exhibiting high ionic conductivities, J. Mol. Liq. 365 (2022) 120126, https://doi.org/10.1016/j.molliq.2022.120126.

[47] S. Sudhakar, T. Narasimhaswamy, K.S.V. Srinivasan, Synthesis, characterization, and thermal properties of 4,4′-bis(4-n-alkoxybenzoyloxy)benzylideneanilines and bis(4- benzylidene-4′-n-alkoxyaniline) terephthalates, Liq. Cryst. 27 (2000) 1525–1532, https://doi.org/10.1080/026782900750018690.

[48] I.-H. Kim, H.-J. Tsai, K. Nishi, T. Kasagami, C. Morisseau, B.D. Hammock, 1,3-Disubstituted ureas functionalized with ether groups are potent inhibitors of the soluble epoxide hydrolase with improved pharmacokinetic properties, J. Med. Chem. 50 (2007) 5217–5226, https://doi.org/10.1021/jm070705c.

[49] G.D. Sharma, D. Saxena, M.S. Roy, Studies on electrical and photoelectrical behaviour of ITO/ArV/In Schottky barrier device, Synth. Met. 106 (1999) 97–105, https://doi.org/10.1016/S0379-6779(99)00115-0.

[50] W.-C. Cheng, M.J. Kurth, The Zincke reaction. A Review, Org. Prep. Proced. Int. 34 (2002) 585–608, https://doi.org/10.1080/00304940209355784.

[51] L. Chen, H. Willcock, C.J. Wedge, F. Hartl, H.M. Colquhoun, B.W. Greenland, Efficient access to conjugated 4,4′-bipyridinium oligomers using the Zincke reaction: synthesis, spectroscopic and electrochemical properties, Org. Biomol. Chem. 14 (2016) 980–988, https://doi.org/10.1039/C5OB02211H.

[52] S. Kumar (Ed.), Liquid Crystals Experimental Study of Physical Properties and Phase Transitions, London, Eng, Cambridge, 2001.

[53] G.W. Gray, J.W.G. Goodby, Smectic Liquid Crystals: Textures and Structures, Leonard Hill, Glasgow, 1984.

[54] P.J. Collins, M. Hird, Introduction to Liquid Crystals Chemistry and Physics, Taylor & Francis, Bristol, PA, 1997.

[55] D. Demus, J.W. Goodby, G.W. Gray, H.-W. Spiess, V. Vill (Eds.), Handbook of Liquid Crystals, Vols. 1–3, Wiley-VCH, Weinheim, Germany, 1998.

[56] I. Dierking, Textures of Liquid Crystals, Wiley-VCH, Weinheim, Germany, 2003.

[57] Handbook of Liquid Crystals: 8 Volume Set, 2nd edition, J.W. Goodby, P.J. Collings, T. Kato, C. Tschierske, H.F. Gleeson, P. Raynes (Eds), Wiley-VCH, Weinheim, Germany, 2014.

[58] S. Xu, Y. Duan, B. Liu, Precise molecular design for high-performance luminogens with aggregation-induced emission, Adv. Mater. 32 (1) (2020) 1903530, https://doi.org/10.1002/adma.201903530.

[59] A.C.B. Rodrigues, J.S.S. de Melo, Aggregation-induced emission: from small molecules to polymers-historical background, mechanisms and photophysics, Top. Curr. Chem. 379 (2021) 15, https://doi.org/10.1007/s41061-021-00327-9.

[60] U.H. Choi, T.L. Price Jr., D.V. Schoonover, R. Xie, H.W. Gibson, R.H. Colby, Role of chain polarity onion and polymer dynamics: Molecular volume-based analysis of the dielectric constant for polymerized norbornene-based ionic liquids, Macromolecules 53 (23) (2020) 10561–10573, https://doi.org/10.1021/acs.macromol.0c02100.

[61] T. Gao, J. Itliong, S.P. Kumar, Z. Hjorth, I. Nakamura, Polarization of ionic liquid and polymer and its implications for polymerized ionic liquids: An overview towards a new theory and simulation, J. Polym. Sci. 59 (21) (2021) 2434–2457, https://doi.org/10.1002/pol.20210330.

[62] P.G. Bruce, C.A. Vincent, Polymer electrolytes, J. Chem. Society, Faraday Trans. 89 (17) (1993) 3178–3203, https://doi.org/10.1039/FT9938903187.

[63] H.J. Jiang, Structural design of ionic liquids for process optimization, Ph.D. Dissertation, 2018, The University of Sydney, Australia.

[64] W.H. Meyer, Polymer electrolytes for lithium-ion batteries, Adv. Mater. 10 (6) (1998) 439–448, https://doi.org/10.1002/(SICI)1521-4095(199804)10:6<C439::AID- ADMA439>E3.0.CO;2-I.

[65] E. Barsoukov, J.R. Macdonald, Impedance Spectroscopy, second ed., Wiley, New York, 2005.

[66] M. Wubbenhorst, J. van Turnhout, Analysis of complex dielectric spectra. I. One-dimensional derivative techniques and three-dimensional modeling, J. Non-Cryst. Solids 305 (2002) 40–49, https://doi.org/10.1016/S0022-3093(02)01086-4.

[67] J. van Turnhout, M. Wübbenhorst, Analysis of complex dielectric spectra. II. Evaluation of the activation energy landscape by differential sampling, J. Non-Cryst. Solids 305 (2002) 50–58, https://doi.org/10.1016/S0022-3093(02)01120-1.

[68] H. Bloom, E. Heymann, The electric conductivity and the activation energy of ionic migration of molten salts and their mixtures, Proc R Soc Lond A Math Phys Sci. 188 (1014) (1947) 392–414, https://doi.org/10.1098/rspa.1947.0016. PMID: 20292492.

[69] K.A. Mauritz, R.B. Moore, State of understanding of Nafion, Chem. Rev. 104 (10) (2004) 4535–4585, https://doi.org/10.1021/cr0207123.

[70] A.C. Luntz, B.D. McCloskey, Nonaqueous Li-Air Batteries: A Status Report, Chem. Rev. 114 (23) (2014) 11721–11750, https://doi.org/10.1021/cr500054y.

[71] A. Concellón, S. Hernández-Ainsa, J. Barberá, P. Romero, J.L. Serrano, M. Marcos, Proton conductive ionic liquid crystalline poly(ethyleneimine) polymers functionalized with oxadiazole, RSC Adv. 8 (2018) 37700–37706, https://doi.org/10.1039/C8RA08253G.

[72] J. Yang, Y. Wang, G. Yang, S. Zhan, New anhydrous proton exchange membranes based on fluoropolymers blend imidazolium poly(aromatic ether ketone)s for high temperature polymer electrolyte fuel cells, Int. J. Hydrogen Energy 43 (17) (2018) 8464–8473, https://doi.org/10.1016/j.ijhydene.2018.03.128.

[73] T. Liang, H.P.C. van Kuringen, D.J. Mulder, S. Tan, Y. Wu, Z. Borneman, K. Nijmeijer, A.P.H.J. Schenning, Anisotropic dye adsorption and anhydrous proton conductivity in smectic liquid crystal networks: The role of cross-link density, order, and orientation, ACS Appl. Mater. Interfaces 9 (40) (2017) 35218–35225, https://doi.org/10.1021/acsami.7b09386.

[74] A.W. Brown, A. Martinez-Felipe, Ionic conductivity mediated by hydrogen bonding in liquid crystalline 4-n-alkoxybenzoic acids, J. Mol. Struct. 1197 (2019) 487–496, https://doi.org/10.1016/j.molstruc.2019.07.072.

[75] S.M. Alauddin, N.F.K. Aripin, T.S. Velayutham, A. Martinez-Felipe, Liquid crystalline copolymers containing sulfonic and light-responsive groups: From molecular design to conductivity, Molecules 25 (11) (2020) 2579, https://doi.org/10.3390/molecules25112579.

[76] S.M. Alauddin, A.R. Ibrahim, N.F.K. Aripin, T.S. Velayutham, O.K. Abou-Zied, A. Martinez-Felipe, New side-chain liquid crystalline terpolymers with anhydrous conductivity: Effect of azobenzene substitution on light response and charge transfer, Eur. Polym. J. 146 (2021) 110246, https://doi.org/10.1016/j.eurpolymj.2020.110246.

[77] L. Vanti, S.M. Alauddin, D. Zaton, N.F.K. Aripin, M. Giacinti-Baschetti, C.T. Imrie, A. Ribes-Greus, A. Martinez-Felipe, Ionically conducting and photoresponsive liquid crystalline terpolymers: Towards multifunctional polymer electrolytes, Eur. Polym. J. 109 (2018) 124–132, https://doi.org/10.1016/j.eurpolymj.2018.08.033.